


Determination of spin Hall angle in the Weyl ferromagnet Co₂MnGa by taking into account the thermoelectric contributions

Hironari Isshiki ^{1,2}, Zheng Zhu,^{1,2} Hayato Mizuno,^{1,2} Ryota Uesugi,^{1,2} Tomoya Higo,^{1,2,3} Satoru Nakatsuji,^{1,2,3,4} and YoshiChika Otani^{1,2,4,5,*}

¹*Institute for Solid State Physics, University of Tokyo, Kashiwa, Chiba 277-8581, Japan*

²*Core Research for Evolutional Science and Technology (CREST), Japan Science and Technology Agency (JST), Saitama 332-0012, Japan*

³*Department of Physics, The University of Tokyo, Bunkyo-ku, Tokyo 113-0033, Japan*

⁴*Trans-scale Quantum Science Institute, University of Tokyo, Bunkyo-ku, Tokyo 113-0033, Japan*

⁵*Center for Emergent Matter Science, RIKEN, Wako, Saitama 51-0198, Japan*



(Received 27 December 2021; revised 22 June 2022; accepted 5 August 2022; published 29 August 2022)

The spin Hall effects of various materials, including Weyl semimetals, have been studied by the spin absorption method with the nonlocal spin valve structures. Here, we study Co₂MnGa (CMG) by using the standard spin absorption method. A considerable amount of thermoelectric signal superimposes on the inverse spin Hall signal in the measurement configuration: the applied electric current between the spin injector (permalloy) and bridge (copper) wires produces heating or cooling at the interface via the Peltier effect, which causes an out-of-plane temperature gradient in CMG. As a result, a voltage signal induced by the anomalous Nernst effect (ANE) of CMG comes into the inverse spin Hall signal. We quantitatively separate these signals by combining the experiment and a numerical simulation. About 75% of the detected signal is found attributable to the thermoelectric effects. The superposing thermoelectric contribution is a general and unavoidable problem in this method when the spin Hall materials exhibit ANE. After eliminating the thermoelectric signal, the spin Hall angle of CMG turns out to be $\theta = -0.09$ at room temperature.

DOI: [10.1103/PhysRevMaterials.6.084411](https://doi.org/10.1103/PhysRevMaterials.6.084411)

I. INTRODUCTION

The spin Hall effect (SHE), generating a pure spin current from an electric current, plays an essential role in switching magnetization via spin-orbit torque in spintronic devices. Thus, conductive materials with significant SHE have been explored for a decade. Recent extensive work has revealed that topological conductors such as topological insulators exhibit an efficient spin-charge interconversion [1–3]. Therefore, it is essential to further extend the frontier of SHE materials to other topological materials. The bulk transport related to the SHE is the anomalous Hall effect (AHE). The dominant part of the AHE in most magnets comes from the intrinsic contribution that arises from Berry curvature in momentum space [4,5]. Hence, the emergence of giant SHE beyond the empirical scaling law can be expected in materials hosting large net Berry curvatures such as Weyl points and nodal lines [6–13]. The full Heusler compound ($L2_1$ -order structured) Co₂MnGa (CMG) exhibits a giant anomalous Nernst effect (ANE) and AHE due to the large Berry curvature as a result of the quantum Lifshitz transition between type-I and II Weyl semimetal [9,14–16].

In recent papers, the spin absorption method with nonlocal spin valve structures (NLSVs) has been adopted to investigate the SHE of the Weyl semimetals [17,18]. This established method enables us to quantitatively determine the spin Hall

angle and spin diffusion length. However, the magnetothermoelectric signals could superimpose on spin Hall signals when spin Hall materials exhibit ANE. This fact seems to be a general problem in this method, although it has been ignored so far. In this paper, we perform the standard spin absorption method on a CMG and show how to quantitatively extract the spin Hall signal by eliminating the magnetothermoelectric signals.

II. MATERIALS AND METHODS

We employ a direct current magnetron sputtering method for growing 30-nm-thick CMG films on MgO(100) substrates at room temperature as described in Ref. [19]. The composition of the CMG [19] is Co:Mn:Ga = 1.98:1.01:1.01. We perform postannealing at 550 °C for 30 min to obtain a flat surface of CMG.

We fabricated standard NLSVs for the spin absorption method where two 30-nm-thick Py (Ni₈₁Fe₁₉) wires and a 30-nm-thick CMG wire in the middle of them are bridged by a 100-nm-thick Cu wire. The distance between two Py wires is 1 μ m. The nanowires were patterned employing the conventional electron beam lithography using ZEP and PMMA resists. The CMG wire was fabricated from the 30-nm-thick film on a MgO substrate by Ar ion etching. Before removing the resist, we deposited 30 nm MgO by electron beam evaporation on top of the etched region to compensate the overarch of the substrate. The resistivity of CMG wire was 288 $\mu\Omega$ cm at room temperature, which

*h_issiki@issp.u-tokyo.ac.jp

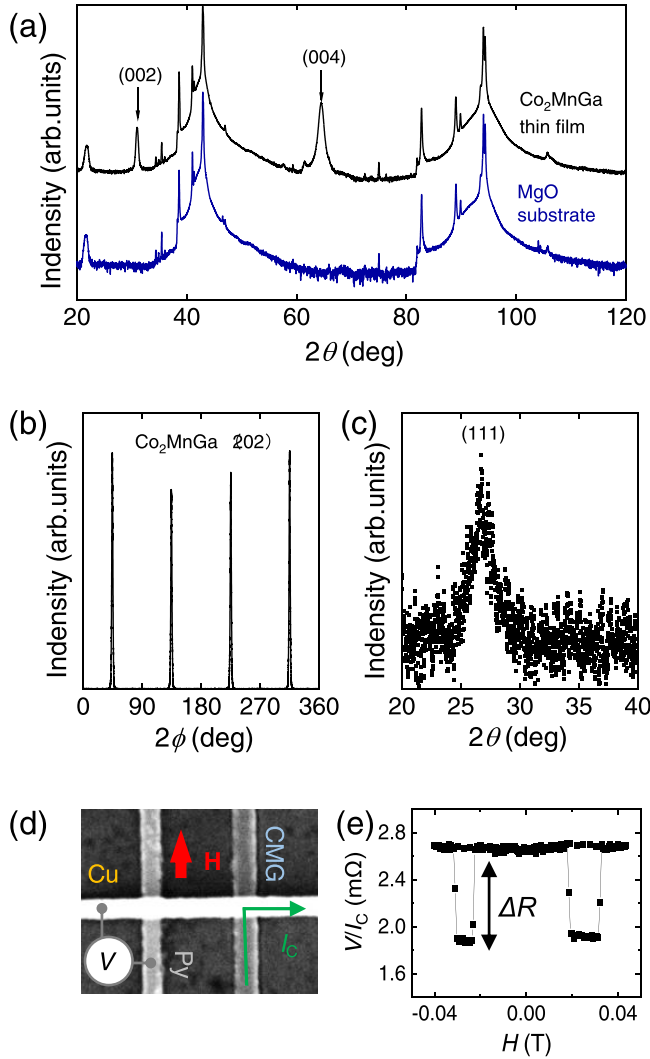


FIG. 1. X-ray diffraction of the Co_2MnGa (CMG) thin film and the nonlocal spin valve. (a) Out-of-plane x-ray diffraction patterns of a $\text{MgO}(001)$ substrate and CMG thin film. (b) ϕ scans for (202) peaks of the CMG thin film. (c) 2θ scan for the superlattice (111) planes of the CMG thin film. (d) The scanning electron microscopy image of the device and the measurement configuration. (e) The nonlocal spin valve signal at 150 K.

decreases monotonically with decreasing temperature. The residual resistivity ratio was ~ 1.04 . The Py wires were deposited under a 10^{-9} Torr base pressure by electron beam evaporation. The 100-nm-thick Cu bridge wire was deposited by a heated tantalum boat under 10^{-10} Torr after the Ar ion beam etching for 30 s to clean the surfaces of CMG and Py wires. The prepared devices were coated with 10-nm-thick Al_2O_3 by RF sputtering to avoid the chemical reaction of the nanowires in the air.

III. RESULTS

A. Crystal structure of CMG and NLSV signal

The x-ray diffraction results of the CMG films are shown in Fig. 1. The (111) superlattice peak indicates the existence of the $L2_1$ -order structure in the CMG film. The degrees of

atomic ordering in the $L2_1$ - and $B2$ -ordered structures are ~ 14 and $\sim 86\%$, respectively, estimated from the intensity ratio of peaks described in Ref. [20]. We prepared NLSV structures [21,22] where the CMG and Py wires are bridged by a Cu wire, namely, Py-CMG NLSV (see the Materials and Methods). The length L between Py and CMG wires is 500 nm. Using the standard lock-in technique, we performed the NLSV measurement using the Py and CMG wires on the configuration shown in Fig. 1(d). The spin injector is CMG, and the detector is Py in this measurement. The typical result at 150 K is shown in Fig. 1(e), where the signal is indicated by the nonlocal resistance given by the voltage signal V divided by the applied current I_c . The square butterfly hysteresis assures a defect-free well-fabricated device. The spin polarization P_{CMG} is estimated to be ~ 0.08 at 150 K and ~ 0.04 at room temperature, much smaller than expected in a half-metallic $L2_1$ -ordered CMG [23,24]. The almost $B2$ -ordered structures in our CMG may cause the small P_{CMG} . Another possible reason is the spin memory loss at the interface that we have ignored in the analysis.

B. Measurement of inverse SHE configuration

Next, as illustrated in Fig. 2(a), we performed experiments using the standard inverse SHE (ISHE) measurement configuration [25–27] with the Py-CMG NLSV structure. In the measurement of ISHE, a spin-polarized electric current is injected from the left Py injector wire to the left end of the Cu wire. Accumulated spins polarized along the spin injector magnetization drive diffusive spin current toward the right at the junction. The spin current diffuses into the CMG wire vertically and generates a charge current via ISHE, which is detected as a voltage between both ends of the CMG wire. The magnetic field is swept along the Cu wire. We show the voltage signals as a function of the magnetic field with positive and negative DC currents $I_c = \pm 500 \mu\text{A}$ at room temperature in Fig. 2(b). The results of the DC measurements consist of two terms that are linear and quadratic to the electric current. The linear term contains the ISHE and the linear thermoelectric effects such as the Peltier effect (PE). The quadratic term should be attributed to the effects induced by Joule heating (JH). To separate these two, we plot half of the difference and the average of the voltage signals with positive and negative DC currents in Fig. 2(c). Half of the difference $V_{\text{DIF}}^{(1)}$ and the average $V_{\text{AVE}}^{(1)}$ represent the signals which are linear and quadratic to the electric current, respectively (the superscripts in $V_{\text{DIF}}^{(1)}$ and $V_{\text{AVE}}^{(1)}$ represent the ISHE configuration). We define the magnitude of signals $2\Delta V_{\text{DIF}}^{(1)}$ and $2\Delta V_{\text{AVE}}^{(1)}$ as the differences between the saturation values at positive and negative magnetic fields. We find that $\Delta V_{\text{DIF}}^{(1)}$ is approximately an order of magnitude larger than that for typical spin Hall materials like Pt [25], consistent with the results in a previous report for $L2_1$ -ordered CMG [18]. Usually, the signal $\Delta V_{\text{DIF}}^{(1)}$ can be attributable solely to the ISHE in measuring paramagnetic spin Hall materials such as Pt. However, if the spin Hall materials in the devices exhibit ANE, magnetothermoelectric effects could smear the ISHE signal.

We discuss the thermoelectric effects linear to the electric current on the ISHE measurement. In the configuration, the applied electric current through the Py-Cu interface at the left

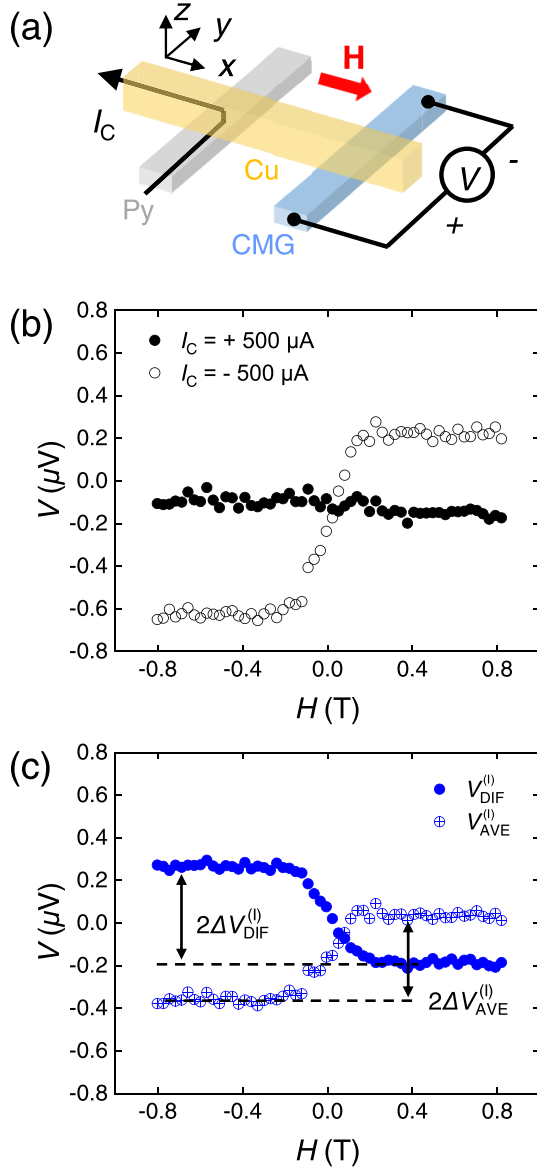


FIG. 2. The measurements of the inverse spin Hall effect (ISHE) of Co_2MnGa with DC currents at 286 K. (a) The configurations for the ISHE measurement. (b) The DC nonlocal voltage signals as a function of the magnetic field with the DC current $I_C = \pm 500 \mu\text{A}$. (c) Half of the difference and the average between the signals with positive and negative DCs.

of the device produces heating or cooling via PE since Py and Cu have different Seebeck coefficients. Due to the high thermal conductivity of Cu, the heat would propagate along the Cu wire to the CMG-Cu junction at the right of the device and flow vertically into the CMG wire. The magnetization of CMG aligned along the Cu wire direction is orthogonal to the temperature gradient; the ANE of CMG causes a voltage between both ends of the CMG wire. Because the PE is proportional to the electric current, the voltage induced by the PE and ANE (PE-ANE) must be linear to the electric current, like the ISHE voltage. By sweeping the magnetic field, the magnetization reversal of the Py and CMG wires should accompany the sign inversions of the ISHE and PE-ANE signals,

TABLE I. Material parameters for the simulation. The thermal conductivities of metals were estimated from the Wiedemann-Franz law [31].

| Materials | ρ ($\mu\Omega \text{ cm}$) | κ (W/mK) | S_{SE} ($\mu\text{V/K}$) |
|---------------|-----------------------------------|-----------------|-------------------------------------|
| Cu | 4.6 | 150 | 1.8 |
| Py | 43 | 16 | -22 [29] |
| CMG | 280 | 2.5 | -15 |
| MgO substrate | | 42 [32] | 0 |
| Amorphous MgO | | 4 [33,34] | 0 |

respectively. However, we cannot distinguish the magnetization reversal of the Py and CMG from this experiment since the magnetic field is applied along the hard magnetic anisotropy axis of these ferromagnetic wires. Therefore, we cannot separate the signals caused by these two different mechanisms:

$$\Delta V_{\text{DIF}}^{(I)} = \Delta V_{\text{ISHE}} + \Delta V_{\text{PE-ANE}}, \quad (1)$$

where ΔV_{ISHE} is the ISHE-induced signal and $\Delta V_{\text{PE-ANE}}$ is the PE-ANE-induced signal. The magnitude of the thermoelectric voltage is given by

$$\Delta V_{\text{PE-ANE}} = -\nabla T_{z, \text{PE}}^{\text{AVE}} \cdot S_{\text{ANE,CMG}} \cdot l_{\text{CMG}}, \quad (2)$$

where $\nabla T_{z, \text{PE}}^{\text{AVE}}$ is the averaged vertical temperature gradient in the CMG wire, l_{CMG} is the length of the CMG wire, and $S_{\text{ANE,CMG}}$ is the transverse Seebeck coefficient of the CMG.

Other than the PE, JH can also be a heat source. The electric current produces JH, and the heat creates a vertical temperature gradient in CMG. Therefore, JH and the ANE (JH-ANE) cause a voltage like the PE-ANE. Since JH is quadratic to the electric current, we would see the signal by JH-ANE in $\Delta V_{\text{AVE}}^{(I)}$:

$$\Delta V_{\text{AVE}}^{(I)} = \Delta V_{\text{JH-ANE}} = -\nabla T_{z, \text{JH}}^{\text{AVE}} \cdot S_{\text{ANE,CMG}} \cdot l_{\text{CMG}}, \quad (3)$$

where $\nabla T_{z, \text{JH}}^{\text{AVE}}$ is the averaged JH-induced vertical temperature gradient. Here, we assume other effects, such as the thermal spin injection from Py, are negligible at room temperature [28,29].

We numerically simulate the temperature distribution in the device caused by the PE and JH using COMSOL Multiphysics [30]. We build a model of the Py-CMG device, which has the same geometry as the real one. The CMG wire fabricated by Ar etching directly contacts the single-crystal MgO substrate in the model. On the other hand, there is a 30-nm-thick amorphous MgO layer between the substrate and wires other than CMG that has been deposited in the fabrication process to compensate for the overetching of the substrate. Here, 10-nm-thick Al_2O_3 was deposited on the device as the capping layer. The material parameters for the simulation are listed in Table I. The initial temperature is 286 K. We plot a simulated spatial temperature distribution induced by the PE and JH separately by applying a positive DC current from Py to Cu wires ($I_C = +500 \mu\text{A}$) in Fig. 3 (we can tune PE and JH on/off separately in the simulation). The results induced by the PE and JH are shown in Figs. 3(a) and 3(c), respectively. We see that there are Peltier cooling on the Py-Cu interface

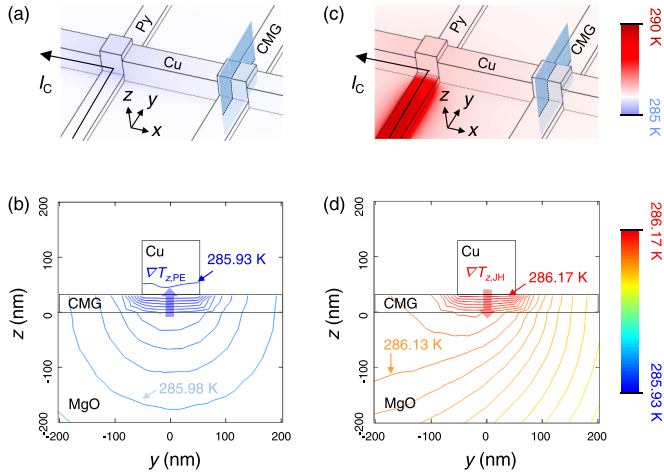


FIG. 3. The simulated temperature distribution induced by the Peltier effect (PE) and Joule heating (JH) in the Py-CMG device at 286 K. The temperature distributions respectively induced by (a) the PE and (c) JH in the device. (b) The PE and (d) JH generated equitemperature maps in the yz cross-sections in the vicinity of the Cu/CMG wire junction marked by the blue rectangular in (a) and (c).

and JH in the Py wire, and these propagate to the right on the device through the Cu wire. The yz cross-sections across the CMG wire are shown in Figs. 3(b) and 3(d). The vertical temperature gradients in the CMG below the Cu wire caused by the PE and JH with $I_c = +500 \mu\text{A}$ are $\sim 8.2 \times 10^5 \text{ K/m}$ and $\sim -9.2 \times 10^5 \text{ K/m}$, respectively. We confirm that the temperature gradient caused by the PE is almost proportional to the electric current, while the gradient caused by JH is proportional to the square of the electric current.

Here, we estimate the signals induced by the PE-ANE $\Delta V_{\text{PE-ANE}}$ to separate it from ΔV_{ISHE} [Eq. (1)]. The signal that is quadratic to the electric current $\Delta V_{\text{AVE}}^{(1)}$ should be induced by the thermal gradient caused by JH. By substituting the experimental value of $\Delta V_{\text{AVE}}^{(1)} = 196 \text{ nV}$ and the simulated value of $\nabla T_{z, \text{JH}}$ for Eq. (3), we obtain the transverse Seebeck coefficient of CMG: $S_{\text{ANE,CMG}} \sim 1.2 \mu\text{V/K}$. This value is reasonable for our CMG consisting of mostly $B2$ -ordered phase since the ANE of conventional ferromagnets should be in the range of $1 < S_{\text{ANE,CMG}} < 2 \mu\text{V/K}$ [7]. Next, by substituting $S_{\text{ANE,CMG}} \sim 1.2 \mu\text{V/K}$ and the simulated value of $\nabla T_{z, \text{PH}}$ for Eq. (2), we obtain $\Delta V_{\text{PE-ANE}} \sim -172 \text{ nV}$, indicating the thermoelectric effects account for $\sim 75\%$ of the whole experimental signal $\Delta V_{\text{DIF}}^{(1)} = -228 \text{ nV}$ (thus, $\Delta V_{\text{ISHE}} = -56 \text{ nV}$). Therefore, the PE-ANE severely affects the signal of the ISHE measurement. Notably, the simulated results depend on the thermal conductivity of the substrate. The simulated vertical temperature gradient would be $\sim 5.2 \times 10^5 \text{ K/m}$, assuming a Si/SiO₂(300 nm) substrate instead of the MgO substrate, which is still not negligible. Therefore, the superposition of the PE-ANE signal is a general problem on the ISHE measurements when the objects exhibit ANE. However, the ANE induced by the vertical temperature gradient has been ignored in previous reports so far [17,18,35]. Instead of that, the ANE induced by the in-plane temperature gradient $\nabla T_{x, \text{PE}}$ has been discussed [29,36,37] on the nonlocal spin valve measurements where the magnetic field is applied along the ferromagnetic

wires (y direction). Note that the in-plane temperature gradient parallel to the magnetic field causes no ANE in the ISHE measurement.

We estimate the spin Hall angle θ of CMG by using the equation as follows [25–27,38–43]:

$$\theta = \frac{w_{\text{CMG}} \Delta V_{\text{ISHE}} \left(\frac{1}{\bar{I}_S} \right)}{x \rho_{xx, \text{CMG}}}, \quad (4)$$

where w_{CMG} is the width of the CMG wire, \bar{I}_S is the effective spin current absorbed into CMG wire, and x is the shunting factor. See the Supplemental Material [44] for the determination of \bar{I}_S . The simulation estimates the shunting factor 0.22, which is reasonable compared with our previous reports on other materials, considering the resistivity: $x = 0.36$ for CuIr [38] and $x = 0.04$ for Mn₃Sn [17]. We obtain the spin Hall angle $\theta \sim -0.09$ at 286 K (-0.05 at 200 K) for the mixture of $\sim 14\%$ $L2_1$ - and 86% $B2$ -ordered CMG. This value is almost consistent with the reported values of ~ -0.079 for $B2$ -ordered CMG estimated from the spin-orbit torque measurement [45]. Unless we eliminated the PE-ANE contribution, we would obtain an incorrect value θ of ~ -0.4 at 286 K. Therefore, we must carefully perform the spin absorption measurement to determine the SHE angle of materials that exhibit ANE.

C. Measurement of SHE configuration

We also perform the SHE measurement using the device. The measurement configuration is shown in Fig. 4(a). The SHE-induced spin current can be detected as a voltage signal between the Py wire and the left end of the Cu wire. The results of DC measurement at room temperature are shown in Fig. 4(b). Like Fig. 2(c), we plot half of the difference and the average of the voltage signals [$V_{\text{DIF}}^{(S)}$ and $V_{\text{AVE}}^{(S)}$] with positive and negative DC currents $I_c = \pm 500 \mu\text{A}$ in Fig. 4(c). Here, $V_{\text{DIF}}^{(S)}$ includes the SHE signal. However, we should consider the anomalous Ettingshausen effect (AEE) and the Seebeck effect (SE), the inverse effects of ANE and PE, respectively. An electric current flows in the CMG wire with its magnetization parallel to the Cu wire, producing a vertical temperature gradient due to the AEE of CMG. The temperature gradient would be translated to a voltage via SE at the Py-Cu interface. Thus, in the SHE configuration, the obtained signal amplitude linear to the electric current should be represented by

$$\Delta V_{\text{DIF}}^{(S)} = \Delta V_{\text{SHE}} + \Delta V_{\text{AEE-SE}}, \quad (5)$$

where ΔV_{SHE} is the SHE-induced signal and $\Delta V_{\text{AEE-SE}}$ is the AEE- and SE-induced signal (AEE-SE). However, we cannot evaluate the value of $\Delta V_{\text{AEE-SE}}$ since COMSOL Multiphysics does not handle AEE (and ANE).

Here, we consider the signal $V_{\text{AVE}}^{(S)}$ in Fig. 4(c) that is quadratic to the electric current. An electric current applied to the CMG wire in the device produces a significant amount of JH due to the high resistivity of the CMG wire ($\sim 290 \mu\Omega \text{ cm}$). The heat increases the temperature at the Py-Cu interface from the equilibrium. The large offset ($\sim -35.3 \mu\text{V}$) of $V_{\text{AVE}}^{(S)}$ reflects the Seebeck voltage, which is reproducible quantitatively by the simulation. JH may create a vertical temperature gradient in the Py wire. The signal amplitude of ANE may appear as $\Delta V_{\text{AVE}}^{(S)}$ (the difference between the saturation values

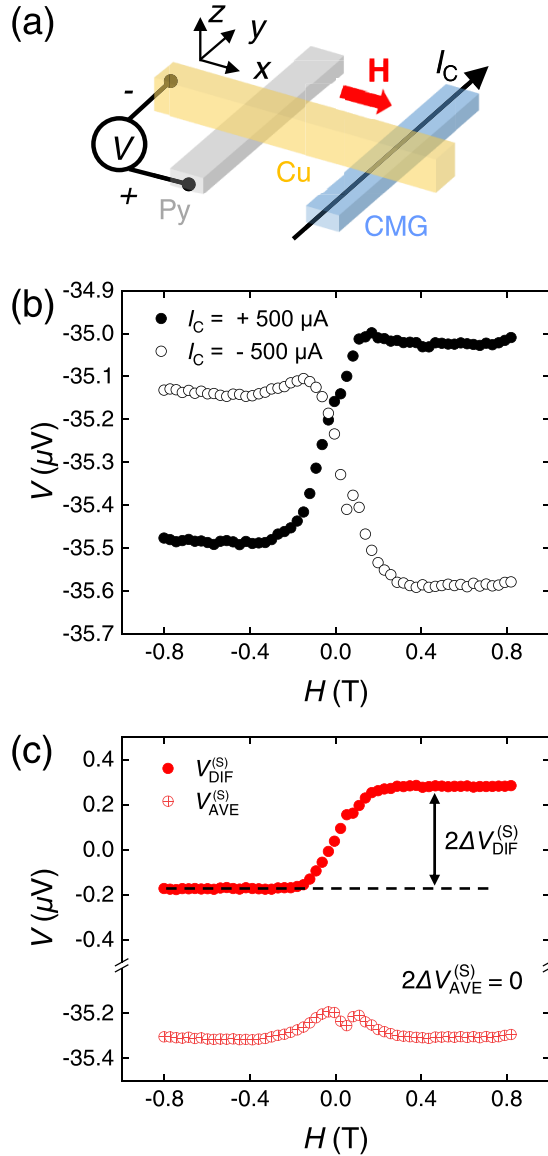


FIG. 4. The measurements of the spin Hall effect (SHE) of Co_2MnGa with DC currents at 286 K. (a) The configurations for the SHE measurement. (b) The DC nonlocal voltage signals as the function of magnetic field with the DC current is $I_c = \pm 500 \mu\text{A}$. (c) Half of the difference and the average between the signals with positive and negative DCs.

at positive and negative magnetic fields) since a relatively large ANE has been reported for Py ($S_{\text{ANE,Py}} \sim 2.6 \mu\text{V/K}$) [37,46,47]. However, in the experiment, the signal $\Delta V_{\text{AVE}}^{(S)}$ is almost zero. According to our simulation, JH increases the temperature of both the Cu wire and the substrate. As a result, the net vertical temperature gradient in the Py wire becomes zero, explaining the experimental results. However, notably, the result of the simulation depends on the geometry of the device. The peak near zero external magnetic fields may be explained: the shape anisotropy aligns the Py magnetization along the wire direction when the magnetic field is small. The in-plane temperature gradient causes the voltage via the ANE or planar Nernst effect of Py that is detectable in the SHE configuration. We also perform ISHE and SHE measurements

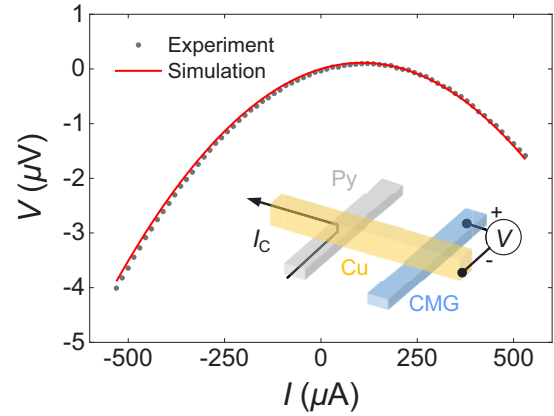


FIG. 5. The nonlocal baseline voltages on the Py-CMG device at 286 K. The inset represents the measurement configuration. The black dots represent the experimental voltage-current curve. The result of the simulation with $S_{\text{SE,CMG}} = -15 \mu\text{V/K}$ are shown as the red curve.

using a CMG-CMG NLSV ($L = 400 \text{ nm}$). The results are shown in the Supplemental Material [44], which are qualitatively consistent to the results with the Py-CMG NLSV.

IV. DISCUSSION

A. Baseline voltage

We measure the nonlocal voltage induced by the PE and SE in the configuration shown in the inset of Fig. 5. In this measurement, we apply a current from the Py wire to the left end of the Cu wire and measure the voltage between the CMG wire and the right end of the Cu wire. The electric current produces Peltier cooling or heating and JH on the left of the device, which changes the temperature at the CMG-Cu junction. As a result, the Seebeck voltage is detected, known as the baseline voltage [48,49]. The baseline voltage (Seebeck voltage) is given by

$$V_{\text{BL}} = (S_{\text{SE,CMG}} - S_{\text{SE,Cu}}) \cdot (T_{\text{inter}} - T_0), \quad (6)$$

where $S_{\text{SE,CMG}}$ and $S_{\text{SE,Cu}}$ are Seebeck coefficients of CMG and Cu, respectively, T_{inter} is the temperature at the interface of CMG and Cu, and T_0 is the reference temperature at the ends of the detector wires. Since $|S_{\text{SE,CMG}}| \gg |S_{\text{ANE,CMG}}|$, we ignore the contribution of the ANE on V_{BL} . We plot an experimental result of the voltage-current curve at 286 K in Fig. 5 by black dots. The linear and quadratic terms are attributable to the voltage induced by the PE and JH, respectively. We attempt to reproduce the voltage-current curve using the simulation with the material parameters shown in Table I. By assuming $S_{\text{SE,CMG}} = -15 \mu\text{V/K}$, the experimental voltage-current curve is well reproduced, as shown by the red curve in Fig. 5. The excellent agreement between the simulated and experimental baseline voltage confirms the validity of the simulation. We also performed the same measurements for the CMG-CMG NLSV. The result is shown in the Supplemental Material [44].

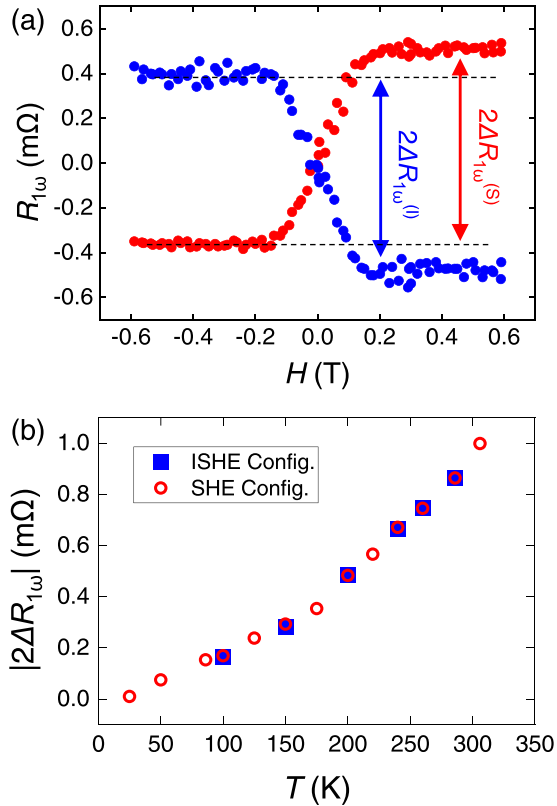


FIG. 6. The nonlocal signals of inverse spin Hall effect (ISHE) and spin Hall effect (SHE). (a) The signals on ISHE (red) and SHE (blue) configurations at 286 K. (b) The temperature dependence of the magnitude of the signals.

B. Reciprocal relation between ISHE and SHE measurements

We investigate the relationship between the signals on the ISHE and SHE measurement configurations. Below, we use the standard lock-in technique by applying an AC current I_{AC} and detecting the first harmonic voltage $V_{1\omega}$: the JH effect has been eliminated. The results of the measurements at room temperature are shown in Fig. 6(a) where nonlocal resistance is defined by $R_{1\omega} \equiv V_{1\omega}/I_{AC}$. The results are consistent with the DC measurements. The temperature dependence of the signal amplitudes $\Delta R_{1\omega}$ are shown in Fig. 6(b). We find that $\Delta R_{1\omega}^{(I)} = -\Delta R_{1\omega}^{(S)}$ holds at all the temperatures in our measurements. A similar relationship has been confirmed in spin absorption measurements for the other paramagnetic spin Hall materials such as Pt and Bi [25], known as the Onsager reciprocal relation [50]. As discussed above, these signals include (I)SHE and thermoelectric signals. Therefore, we experimentally demonstrate that Onsager reciprocal relation is valid for

TABLE II. The detectable signals in ISHE and SHE configurations.

| | ISHE configuration | SHE configuration |
|--------------------|--------------------|-------------------|
| Linear to I_c | ISHE PE-ANE | SHE AEE-SE |
| Quadratic to I_c | JH-ANE | JH-ANE |

the SHE, ISHE, PE-ANE, and AEE-SE. Our results imply that the thermoelectric effects may contribute to the signal $R_{1\omega}$ even though the Onsager reciprocal relation takes place between the ISHE and SHE measurements. We summarize the effects that are detectable in each configuration in Table II. On the other hand, Leiva *et al.* [18] claimed the lack of the Onsager reciprocal relationship in their results on a CMG-CMG NLSV. However, we cannot directly compare our results with theirs since their CMG has the $L2_1$ -ordered phase.

Additionally, there is a characteristic temperature dependence in the magnitude of the nonlocal resistances. The signals $|\Delta R_{1\omega}|$ decrease with decreasing temperature. The decay of the signals with decreasing temperature should be mainly attributable to the temperature dependence of the thermoelectric effects since the absolute values of the Seebeck coefficient Py and the transverse Seebeck coefficient of CMG generally decrease with decreasing temperature [29,51].

V. CONCLUSIONS

In this paper, we studied the SHE and its inverse of CMG using the spin absorption method with NLSVs with Py wires as the spin detector and injector. We found the superimposing magnetothermoelectric signal induced by the PE and ANE on the inverse spin Hall signals. Combining the experimental results and the simulation using COMSOL Multiphysics, we estimate the size of the thermoelectric effect quantitatively, which is $\sim 75\%$ of the whole signal. This superposing magnetothermoelectric contribution has not been discussed yet, but it is a general and unavoidable problem in this method when spin Hall materials exhibit ANE. After eliminating the thermoelectric effects, we found that the spin Hall angle of CMG is determined to be ~ -0.09 at room temperature.

ACKNOWLEDGMENTS

This paper was partially supported by JST-Mirai Program (Grant No. JPMJMI20A1) CREST (Grant No. JPMJCR18T3) from JST, JSPS KAKENHI Grants No. 19K23423, No. 19H05629, No. 19K15431, and No. 19H00650.

- [1] K. Kondou, R. Yoshimi, A. Tsukazaki, Y. Fukuma, J. Matsuno, K. S. Takahashi, M. Kawasaki, Y. Tokura, and Y. Otani, Fermi-level-dependent charge-to-spin current conversion by Dirac surface states of topological insulators, *Nat. Phys.* **12**, 1027 (2016).
- [2] M. DC, R. Grassi, J.-Y. Chen, M. Jamali, D. Reifsnnyder Hickey, D. Zhang, Z. Zhao, H. Li, P. Quarterman, Y. Lv *et al.*, Room-

temperature high spin-orbit torque due to quantum confinement in sputtered $\text{Bi}_x\text{Se}_{(1-x)}$ films, *Nat. Mater.* **17**, 800 (2018).

- [3] H. He, L. Tai, H. Wu, D. Wu, A. Razavi, T. A. Gosavi, E. S. Walker, K. Oguz, C.-C. Lin, K. Wong, Y. Liu *et al.*, Conversion between spin and charge currents in topological-insulator/nonmagnetic-metal systems, *Phys. Rev. B* **104**, L220407 (2021).

- [4] N. Nagaosa, J. Sinova, S. Onoda, A. H. MacDonald, and N. P. Ong, Anomalous Hall effect, *Rev. Mod. Phys.* **82**, 1539 (2010).
- [5] D. Xiao, M.-C. Chang, and Q. Niu, Berry phase effects on electronic properties, *Rev. Mod. Phys.* **82**, 1959 (2010).
- [6] S. Nakatsuji, N. Kiyohara, and T. Higo, Large anomalous Hall effect in a non-collinear antiferromagnet at room temperature, *Nature (London)* **527**, 212 (2015).
- [7] M. Ikhlas, T. Tomita, T. Koretsune, M. T. Suzuki, D. Nishio-Hamane, R. Arita, Y. Otani, and S. Nakatsuji, Large anomalous Nernst effect at room temperature in a chiral antiferromagnet, *Nat. Phys.* **13**, 1085 (2017).
- [8] X. Li, L. Xu, L. Ding, J. Wang, M. Shen, X. Lu, Z. Zhu, and K. Behnia, Anomalous Nernst and Righi-Leduc Effects in Mn_3Sn : Berry Curvature and Entropy Flow, *Phys. Rev. Lett.* **119**, 056601 (2017).
- [9] A. Sakai, Y. P. Mizuta, A. A. Nugroho, R. Sihombing, T. Koretsune, M.-T. Suzuki, N. Takemori, R. Ishii, D. Nishio-Hamane, R. Arita *et al.*, Giant anomalous Nernst effect and quantum-critical scaling in a ferromagnetic semimetal, *Nat. Phys.* **14**, 1119 (2018).
- [10] E. Liu, Y. Sun, N. Kumar, L. Muechler, A. Sun, L. Jiao, S.-Y. Yang, D. Liu, A. Liang, Q. Xu *et al.*, Giant anomalous Hall effect in a ferromagnetic kagome-lattice semimetal, *Nat. Phys.* **14**, 1125 (2018).
- [11] S. N. Guin, S. N. Guin, P. Vir, Y. Zhang, N. Kumar, S. J. Watzman, C. Fu, E. Liu, K. Manna, W. Schnelle *et al.*, Zero-field Nernst effect in a ferromagnetic kagome-lattice Weyl-semimetal Co_3Sn_2S , *Adv. Mater.* **31**, 1806622 (2019).
- [12] A. Sakai, S. Minami, T. Koretsune, T. Chen, T. Higo, Y. Wang, T. Nomoto, M. Hirayama, S. Miwa, D. Nishio-Hamane *et al.*, Iron-Based binary ferromagnets for transverse thermoelectric conversion, *Nature (London)* **581**, 53 (2020).
- [13] T. Chen, T. Tomita, S. Minami, M. Fu, T. Koretsune, M. Kitatani, I. Muhammad, D. Nishio-Hamane, R. Ishii, F. Ishii *et al.*, Anomalous transport due to Weyl fermions in the chiral antiferromagnets Mn_3X , $X = Sn, Ge$, *Nat. Commun.* **12**, 572 (2021).
- [14] I. Belopolski, K. Manna, D. S. Sanchez, G. Chang, B. Ernst, J. Yin, S. S. Zhang, T. Cochran, N. Shumiya, H. Zheng *et al.*, Discovery of topological Weyl fermion lines and drum-head surface states in a room temperature magnet, *Science* **365**, 1278 (2019).
- [15] K. Sumida, Y. Sakuraba, K. Masuda, T. Kono, M. Kakoki, K. Goto, W. Zhou, K. Miyamoto, Y. Miura, T. Okuda *et al.*, Spin-Polarized Weyl cones and giant anomalous Nernst effect in ferromagnetic Heusler films, *Commun. Mater.* **1**, 89 (2020).
- [16] L. Xu, X. Li, L. Ding, T. Chen, A. Sakai, B. Fauqué, S. Nakatsuji, Z. Zhu, and K. Behnia, Anomalous transverse response of Co_2MnGa and universality of the room-temperature $\alpha_{ij}^A/\sigma_{ij}^A$ ratio across topological magnets, *Phys. Rev. B* **101**, 180404(R) (2020).
- [17] P. K. Muduli, T. Higo, T. Nishikawa, D. Qu, H. Isshiki, K. Kondou, D. Nishio-Hamane, S. Nakatsuji, and Y. Otani, Evaluation of spin diffusion length and spin Hall angle of the antiferromagnetic Weyl semimetal Mn_3Sn , *Phys. Rev. B* **99**, 184425 (2019).
- [18] L. Leiva, S. Granville, Y. Zhang, S. Dushenko, E. Shigematsu, T. Shinjo, R. Ohshima, Y. Ando, and M. Shiraishi, Giant spin Hall angle in the Heusler alloy Weyl ferromagnet Co_2MnGa , *Phys. Rev. B* **103**, L041114 (2021).
- [19] Z. Zhu, T. Higo, S. Nakatsuji, and Y. Otani, Magnetic and transport properties of Amorphous, $B2$ and $L2_1$ Co_2MnGa thin films, *AIP Adv.* **10**, 085020 (2020).
- [20] Y. Takamura, R. Nakane, and S. Sugahara, Analysis of $L2_1$ -ordering in full-Heusler Co_2FeSi alloy thin films formed by rapid thermal annealing, *J. Appl. Phys.* **105**, 07B109 (2009).
- [21] F. J. Jedema, M. S. Nijboer, A. T. Filip, and B. J. van Wees, Spin injection and spin accumulation in all-metal mesoscopic spin valves, *Phys. Rev. B* **67**, 085319 (2003).
- [22] T. Kimura, J. Hamrle, Y. Otani, K. Tsukagoshi, and Y. Aoyagi, Spin-dependent boundary resistance in the lateral spin-valve structure, *Appl. Phys. Lett.* **85**, 3501 (2004).
- [23] J. C. Tung and G. Y. Guo, High spin polarization of the anomalous Hall current in Co-based heusler compounds, *New J. Phys.* **15**, 033014 (2013).
- [24] M. Kolbe, S. Chadov, E. A. Jorge, G. Schönhense, C. Felser, H.-J. Elmers, M. Kläui, and M. Jourdan, Test of band structure calculations for Heusler compounds by spin-resolved photoemission spectroscopy, *Phys. Rev. B* **86**, 024422 (2012).
- [25] M. Morota, Y. Niimi, K. Ohnishi, D. H. Wei, T. Tanaka, H. Kontani, T. Kimura, and Y. Otani, Indication of intrinsic spin Hall effect in $4d$ and $5d$ transition metals, *Phys. Rev. B* **83**, 174405 (2011).
- [26] Y. Niimi, H. Suzuki, Y. Kawanishi, Y. Omori, T. Valet, A. Fert, and Y. Otani, Extrinsic spin Hall effects measured with lateral spin valve structures, *Phys. Rev. B* **89**, 054401 (2014).
- [27] Y. Niimi, Y. Kawanishi, D. H. Wei, C. Deranlot, H. X. Yang, M. Chshiev, T. Valet, A. Fert, and Y. Otani, Giant Spin Hall Effect Induced by Skew Scattering from Bismuth Impurities Inside Thin Film CuBi Alloys, *Phys. Rev. Lett.* **109**, 156602 (2012).
- [28] S. Hu, H. Itoh, and T. Kimura, Efficient thermal spin injection using CoFeAl nanowire, *NPG Asia Mater.* **6**, e127 (2014).
- [29] S. Hu, J. Zhao, L. Wang, X. Cui, K. Ohnishi, T. Ariki, T. Min, K. Xia, and T. Kimura, Substantial enhancement of thermal spin polarization in Py/Cu interface, *Phys. Rev. Materials* **2**, 104403 (2018).
- [30] COMSOL Multiphysics® v. 6.0. www.comsol.com. COMSOL AB, Stockholm, Sweden.
- [31] A. D. Avery, S. J. Mason, D. Bassett, D. Wesenberg, and B. L. Zink, Thermal and electrical conductivity of approximately 100-nm Permalloy, Ni, Co, Al, and Cu films and examination of the Wiedemann-Franz law, *Phys. Rev. B* **92**, 214410 (2015).
- [32] G. A. Slack, Thermal conductivity of MgO , Al_2O_3 , $MgAl_2O_4$, and Fe_3O_4 crystals from 3° to $300^\circ K$, *Phys. Rev.* **126**, 427 (1962).
- [33] S. M. Lee, D. G. Cahill, and T. H. Allen, Thermal conductivity of sputtered oxide films, *Phys. Rev. B* **52**, 253 (1995).
- [34] T. Huebner, U. Martens, J. Walowski, M. Münzenberg, A. Thomas, G. Reiss, and T. Kuschel, Thermal conductivity of thin insulating films determined by tunnel magneto-Seebeck effect measurements and finite-element modeling, *J. Phys. D: Appl. Phys.* **51**, 224006 (2018).
- [35] Y. Omori, E. Sagasta, Y. Niimi, M. Gradhand, L. E. Hueso, F. Casanova, and Y. C. Otani, Relation between spin Hall effect and anomalous Hall effect in $3d$ ferromagnetic metals, *Phys. Rev. B* **99**, 014403 (2019).

- [36] A. Hojem, D. Wesenberg, and B. L. Zink, Thermal spin injection and interface insensitivity in permalloy/aluminum metallic nonlocal spin valves, *Phys. Rev. B* **94**, 024426 (2016).
- [37] R. K. Bennet, A. Hojem, and B. L. Zink, Temperature dependence of the anomalous Nernst coefficient for $\text{Ni}_{80}\text{Fe}_{20}$ determined with metallic nonlocal spin valves, *AIP Adv.* **10**, 065127 (2020).
- [38] Y. Niimi, M. Morota, D. H. Wei, C. Deranlot, M. Basletic, A. Hamzic, A. Fert, and Y. Otani, Extrinsic Spin Hall Effect Induced by Iridium Impurities in Copper, *Phys. Rev. Lett.* **106**, 126601 (2011).
- [39] K. Fujiwara, Y. Fukuma, J. Matsuno, H. Idzuchi, Y. Niimi, Y. Otani, and H. Takagi, *5d* iridium oxide as a material for spin-current detection, *Nat. Commun.* **4**, 2893 (2013).
- [40] P. Laczkowski, J.-C. Rojas-Sánchez, W. Saverio-Torres, H. Jaffrès, N. Reyren, C. Deranlot, L. Notin, C. Beigné, A. Marty, J.-P. Attané *et al.*, Experimental evidences of a large extrinsic spin Hall effect in AuW alloy, *Appl. Phys. Lett.* **104**, 142403 (2014).
- [41] M. Isasa, E. Villamor, L. E. Hueso, M. Gradhand, and F. Casanova, Temperature dependence of spin diffusion length and spin Hall angle in Au and Pt, *Phys. Rev. B* **91**, 024402 (2015).
- [42] E. Sagasta, Y. Omori, M. Isasa, M. Gradhand, L. E. Hueso, Y. Niimi, Y. C. Otani, and F. Casanova, Tuning the spin Hall effect of Pt from the moderately dirty to the superclean regime, *Phys. Rev. B* **94**, 060412(R) (2016).
- [43] H. Isshiki, P. Muduli, J. Kim, K. Kondou, and Y. C. Otani, Phenomenological model for the direct and inverse Edelstein effects, *Phys. Rev. B* **102**, 184411 (2020).
- [44] See Supplemental Material at <http://link.aps.org/supplemental/10.1103/PhysRevMaterials.6.084411> for the details of the experiments.
- [45] K. Tang, Z. Wen, Y.-C. Lau, H. Sukegawa, T. Seki, and S. Mitani, Magnetization switching induced by spin-orbit torque from Co_2MnGa magnetic Weyl semimetal thin films, *Appl. Phys. Lett.* **118**, 062402 (2021).
- [46] A. Slachter, F. L. Bakker, and B. J. van Wees, Anomalous Nernst and anisotropic magnetoresistive heating in a lateral spin valve, *Phys. Rev. B* **84**, 020412(R) (2011).
- [47] R. K. Bennet, A. Hojem, and B. L. Zink, Thermal gradients and anomalous Nernst effects in membrane-supported nonlocal spin valves, *Phys. Rev. B* **100**, 104404 (2019).
- [48] F. L. Bakker, A. Slachter, J.-P. Adam, and B. J. van Wees, Interplay of Peltier and Seebeck Effects in Nanoscale Nonlocal Spin Valves, *Phys. Rev. Lett.* **105**, 136601 (2010).
- [49] S. Kasai, S. Hirayama, Y. K. Takahashi, S. Mitani, K. Hono, H. Adachi, J. Ieda, and S. Maekawa, Thermal engineering of non-local resistance in lateral spin valves, *Appl. Phys. Lett.* **104**, 162410 (2014).
- [50] L. Onsager, Reciprocal relations in irreversible Processes. I., *Phys. Rev.* **37**, 405 (1931).
- [51] S. N. Guin, K. Manna, J. Noky, S. J. Watzman, C. Fu, N. Kumar, W. Schnelle, C. Shekhar, Y. Sun, J. Gooth *et al.*, Anomalous Nernst effect beyond the magnetization scaling relation in the ferromagnetic Heusler compound Co_2MnGa , *NPG Asia Mater.* **11**, 16 (2019).